## Fluorescence via Reverse Intersystem Crossing from Higher Triplet States in a Bisanthracene Derivative

Tohru Sato\*

Department of Molecular Engineering,

Graduate School of Engineering, Kyoto University,

Nishikyo-ku, Kyoto 615-8510, Japan and

Unit of Elements Strategy Initiative for Catalysts & Batteries,

Kyoto University, Nishikyo-ku, Kyoto 615-8510, Japan

## Rika Hayashi

Undergraduate School of Industrial Chemistry,
Faculty of Engineering, Kyoto University,
Nishikyo-ku, Kyoto 615-8510, Japan

## Naoki Haruta

Department of Molecular Engineering,

Graduate School of Engineering, Kyoto University,

Nishikyo-ku, Kyoto 615-8510, Japan

#### Yong-Jin Pu

Department of Organic Device Engineering and Research Center for Organic Electronics,

Yamagata University, 4-3-16, Johnan, Yonezawa, 992-8510, Japan and

PRESTO (Sakiqake), JST

(Dated: September 21, 2016)

## Abstract

To elucidate the high external quantum efficiency observed for organic light-emitting diodes using a bisanthracene derivative, BD1, as the emitting molecule, off-diagonal vibronic coupling constants (VCCs) between the excited states of BD1, which govern non-radiative transition rates, were calculated employing time-dependent density functional theory. The VCCs were analysed based on the concept of vibronic coupling density. The VCC calculations suggest a fluorescence via higher triplets (FvHT) mechanism, which entails the conversion of a T<sub>4</sub> exciton generated during electrical excitation into an  $S_2$  exciton via reverse intersystem crossing (RISC); moreover, the  $S_2$  exciton relaxes to a fluorescent  $S_1$  exciton because of large vibronic coupling between  $S_2$  and  $S_1$ . This mechanism is valid as long as the relaxation of triplet states higher than  $T_1$  to lower states is suppressed. The symmetry-controlled thermally activated delayed fluorescence (SC-TADF) and inverted singlet and triplet (iST) structure, which have been proposed in our previous studies, are the special examples of the FvHT mechanism that need high molecular symmetry. However, BD1 achieves the FvHT mechanism in spite of its asymmetrical structure. A general condition for the suppression of radiative and non-radiative transitions in molecules with pseudo-degenerate electronic structures such as BD1 is discussed. A superordinate concept, fluorescence via RISC, which includes TADF, SC-TADF, iST structure, and FvHT is also proposed.

 $<sup>^*</sup>$ tsato@moleng.kyoto-u.ac.jp

#### I. INTRODUCTION

Thermally activated delayed fluorescence (TADF) has attracted significant attention as the emission mechanism in molecules used in organic light-emitting diodes (OLEDs)[1]. Although the phenomenon of TADF has been known for a long time, its application in OLEDs was first reported by Endo *et al.* in 2009[2]. TADF OLEDs utilize fluorescence via reverse intersystem crossing (RISC) from the triplet state,  $T_1$ , generated during electrical excitation, as well as fluorescence from the singlet excited state,  $S_1$ , generated during electrical excitation.

In order to make RISC possible in a molecule, the energy difference between  $S_1$  and  $T_1$ ,  $\Delta E_{ST}$ , must be small enough that the RISC energy barrier can be overcome through thermal excitation.  $\Delta E_{ST}$  can be written as

$$\Delta E_{\rm ST} = 2J = 2 \int \int \psi_{\rm HO}^*(\boldsymbol{r}_1) \psi_{\rm LU}(\boldsymbol{r}_1) \frac{1}{r_{12}} \psi_{\rm HO}(\boldsymbol{r}_2) \psi_{\rm LU}^*(\boldsymbol{r}_2) d^3 \boldsymbol{r}_1 d^3 \boldsymbol{r}_2, \tag{1}$$

where J is an exchange integral, and  $\psi_{\text{HO}}(\mathbf{r})$  and  $\psi_{\text{LU}}(\mathbf{r})$  denote the HOMO and LUMO, respectively. Based on this equation, Endo et~al. proposed a design principle to reduce  $\Delta E_{\text{ST}}[2]$ , i.e. candidates for TADF molecules must be donor-acceptor systems with small overlap between the HOMO and LUMO.

Based on this design principle for emitting molecules, a number of TADF OLEDs have exhibited very high external quantum efficiencies (EQEs). For example, a phenoxazine derivative, PXZ-TRZ, exhibits an EQE of 12.5 % (photoluminescence quantum efficiency (PLQE): 65.7 %)[3], a carbazolyl dicyanobenzene derivative, 4CzIPN, exhibits an EQE of 19.3 % (PLQE: 94 %)[4], a triazine derivative, CC2TA, exhibits an EQE of 11 % (PLQE: 62 %)[5], a spiro bifluorene derivative, Spiro-CN, exhibits an EQE of 4.4 % (PLQE: 27 %)[6], and an acridine derivative, ACRFLCN, exhibits an EQE of 10.1 % (PLQE: 67 %)[7]. Recently, Kaji et al. reported a triazine derivative, DACT-II, exhibiting an extremely high EQE of 41.5 % (PLQE:100 %)[8]. These results demonstrate the success of this design principle.

However, this design principle also has certain drawbacks: (1) the small overlap between the HOMO and LUMO leads to suppression of the oscillator strength[9, 10], and (2) TADF OLEDs exhibit broad emission wavelengths because of charge-transfer (CT) excitation.

In order to overcome these drawbacks, Sato *et al.* proposed other concepts for emitting molecules in OLEDs, viz. symmetry-controlled TADF (SC-TADF) and inverted singlet and

triplet (iST) structure, wherein fluorescence via RISC from triplet states higher than  $T_1$  is utilized based on the selection rules of transition dipole moment (TDM) and spin-orbit coupling (SOC) [11]. The order of the preferable point groups for realizing SC-TADF and iST is as follows:

$$D_{6h} > O_h > I_h = D_{4h} > D_{2h} > D_{3h} > T_d > C_i$$

$$= C_{2h} > D_{2d} = C_{4v} > D_2 = C_{2v} > C_{3v} > C_s = C_1.$$
(2)

These mechanisms are unlike TADF because they enable us to (1) use candidates not belonging to the donor-acceptor type and (2) induce RISC without thermal excitation. Ue-jima et al. and Sato et al. have already designed and proposed iST molecules based on anthracene[9, 10] and perylene derivatives[11], respectively.

Even for asymmetric molecules, RISC via higher  $T_n$  is possible as long as undesirable interactions are suppressed. Recently, a phenothiazin-benzothiadiazole derivative, PTZ-BZP, used as a fluorescent OLED exhibited a high EQE of 1.54 % (PLQE:16 %)[12], which was attributed to fluorescence via RISC from  $T_3$  based on the energy gap law. Sato also proposed that the high EQE in PTZ-BZP, which is an asymmetric molecule, can be attributed to suppressed radiative and non-radiative transitions from triplet states higher than  $T_1$  to lower triplet states because of small overlap densities in the pseudo-degenerate electronic structure as well as the small energy gap between the relevant triplet and singlet states[13].

The overlap density is related to the rate constants of radiative and non-radiative transitions as follows. The rate constant of the radiative transition between electronic states m and n depends on the square of TDM,  $\mu_{mn}$ , defined as

$$\boldsymbol{\mu}_{mn} := \int \cdots \int \Psi_m^*(\boldsymbol{R}_0, \boldsymbol{r}) \left( \sum_i -e \boldsymbol{r}_i \right) \Psi_n(\boldsymbol{R}_0, \boldsymbol{r}) d^4 \boldsymbol{x}_1 \cdots d^4 \boldsymbol{x}_N, \tag{3}$$

while that of the non-radiative transition via vibrational mode  $\alpha$  between vibronic states depends on the square of off-diagonal vibronic coupling constant (VCC)  $V_{\alpha}^{mn}$ , defined as

$$V_{\alpha}^{mn} := \int \cdots \int \Psi_{m}^{*}(\boldsymbol{R}_{0}, \boldsymbol{r}) \left( \frac{\partial \hat{H}}{\partial Q_{\alpha}} \right)_{\boldsymbol{R}_{0}} \Psi_{n}(\boldsymbol{R}_{0}, \boldsymbol{r}) d^{4}\boldsymbol{x}_{1} \cdots d^{4}\boldsymbol{x}_{N}, \tag{4}$$

where  $\hat{H}$  is a molecular Hamiltonian,  $Q_{\alpha}$  stands for a mass-weighted normal coordinate of mode  $\alpha$ ,  $\mathbf{R}_0$  denotes a reference nuclear configuration,  $\mathbf{x}_i = (\mathbf{r}_i, s_i)$  with spatial coordinate  $\mathbf{r}_i$  and spin coordinate  $s_i$  for electron i, e is the elementary charge, and  $\Psi_m$  and  $\Psi_n$  are the

N-electron wave functions of electronic states m and n, respectively [9, 10]. TDM  $\mu_{mn}$  and off-diagonal VCC  $V_{\alpha}^{mn}$  represent the strengths of radiative and non-radiative transitions, respectively. The relations of the radiative and non-radiative transition rate constants to  $\mu_{mn}$  and  $V_{\alpha}^{mn}$  are described in more detail in SEC. S1 of the SM [14].

Both TDM  $\mu_{mn}$  and off-diagonal VCC  $V_{\alpha}^{mn}$  are related to the overlap density  $\rho^{mn}(\mathbf{r}_i)[9, 10]$ . The overlap density  $\rho^{mn}$  is defined by

$$\rho^{mn}(\boldsymbol{r}_i) := N \int \cdots \int \Psi_m^*(\boldsymbol{R}_0, \boldsymbol{r}) \Psi_n(\boldsymbol{R}_0, \boldsymbol{r}) d^4 \boldsymbol{x}_1 \cdots d^4 \boldsymbol{x}_{i-1} ds_i d^4 \boldsymbol{x}_{i+1} \cdots d^4 \boldsymbol{x}_N.$$
 (5)

Hereafter  $\mathbf{r}_i$  is simply denoted as  $\mathbf{r}$ .  $\rho^{mn}(\mathbf{r})$  is sometimes called a transition density, especially within the orbital approximation. For example, in the case of the HOMO-LUMO transition, it is equal to HOMO-LUMO overlap density. The off-diagonal VCC  $V_{\alpha}^{mn}$  can be exactly expressed using the off-diagonal vibronic coupling density (VCD)  $\eta_{\alpha}^{mn}(\mathbf{r})$ :

$$V_{\alpha}^{mn} = \int \eta_{\alpha}^{mn}(\mathbf{r}) d^3 \mathbf{r}, \tag{6}$$

where the off-diagonal VCD is defined by

$$\eta_{\alpha}^{mn}(\mathbf{r}) := \rho^{mn}(\mathbf{r}) \times v_{\alpha}(\mathbf{r}), \tag{7}$$

and the potential derivative  $v_{\alpha}(\mathbf{r})$  is defined by

$$v_{\alpha}(\mathbf{r}) := \left(\frac{\partial u(\mathbf{r})}{\partial Q_{\alpha}}\right)_{\mathbf{R}_{0}}, \quad u(\mathbf{r}) := \sum_{A=1}^{M} -\frac{Z_{A}e^{2}}{4\pi\epsilon_{0}|\mathbf{r} - \mathbf{R}_{A}|},$$
 (8)

where  $u(\mathbf{r})$  is the attractive potential of a single electron due to all nuclei, and  $\mathbf{R}_A$  and  $Z_A$  are the position and charge, respectively of nucleus A. VCD  $\eta_{\alpha}^{mn}(\mathbf{r})$  illustrates the origin of VCC which gives rise to non-radiative transition as a local picture. The detailed derivation of VCD can be found in SEC. S2 of the SM. TDM  $\boldsymbol{\mu}_{mn}$  is also related to the overlap density:

$$\boldsymbol{\mu}_{mn} = \int \boldsymbol{\tau}_{mn}(\boldsymbol{r}) d^3 \boldsymbol{r}, \tag{9}$$

where the transition dipole moment density (TDMD)  $\tau_{mn}(r)$  is defined by

$$\boldsymbol{\tau}_{mn}(\boldsymbol{r}) := -e\boldsymbol{r}\rho^{mn}(\boldsymbol{r}). \tag{10}$$

TDMD  $\tau_{mn}(\mathbf{r})$  illustrates the origin of TDM which causes radiative transition as a local picture. The detailed derivation of TDMD is shown in SEC. S2 of the SM. Based on Eqs. 6,

7, 9, and 10, both radiative and non-radiative transitions are suppressed, when the overlap density  $\rho^{mn}(\mathbf{r})$  is so small that VCD  $\eta_{\alpha}^{mn}(\mathbf{r})$  and TDMD  $\boldsymbol{\tau}_{mn}(\mathbf{r})$  are small.

Hu et al. observed blue-light emission in OLEDs using bisanthracene derivatives including 1,4-bis(10-phenylanthracene-9-yl)benzene (BD1) (see FIG. 1)[15]. Since the observed PLQE

FIG. 1. Bisanthracene derivative, BD1.

of BD1 is 14% in the neat film while the maximum EQE is 8.9% in the doped film, the emission is not conventional fluorescence using only singlet excitons. In other words, triplet excitons must contribute to the observed emission. One possible mechanism to explain the observed high EQE is the triplet-triplet annihilation (TTA). In the TTA mechanism, 62.5% of generated excitons can be up-converted into the singlet excited state at best. Hu et al. have reported that, for example, the highest EQE value is 5.6% in the device employing a neat film of BD1 as an emitting layer, and the observed PLQE of the neat film is 14% [15]. Using these values, the estimated upper-limit of the EQE is 1.8%–3.5% if the outcoupling efficiency is assumed to be 20%–40%. Therefore, we cannot explain the observed EQE on the basis of the TTA mechanism.

In this study, we theoretically investigate the mechanism of light emission from an OLED using a bisanthracene derivative, BD1, as the emitting molecule based on the concept of VCD. We propose a fluorescence via higher triplets (FvHT) mechanism to explain the high EQE in OLEDs using BD1, which is valid as long as undesirable radiative and non-radiative transitions are suppressed. In addition, we propose a general condition for the suppression of radiative and non-radiative transitions in molecules with pseudo-degenerate electronic structures such as BD1. In our previous work on PTZ-BZP, we have mentioned that the observed EQE is due to its pseudo degenerate electronic structure. In this study, we perform the analyses for electronic wave functions of BD1 in detail to obtain general design principles for the realization of the present mechanism. The present article consists of the following sections: The method of calculation is described in SEC. II. In SEC. III A, the results for the

Franck-Condon (FC) states are discussed. The optimized structures for the excited states are discussed in SEC. III B. The frontier orbitals and orbital overlap densities are discussed in SEC. III C. In SEC. III D, the selection rules for the couplings are described. The excited states at the optimized structures for the excited states are discussed in SEC. III E. The calculated VCCs are presented in SEC. III F. The obtained VCCs are discussed on the basis of the concept of VCD in SEC. III G. The disappearance of the overlap densities is discussed in SEC. III H. We also present a general condition for the suppression of the radiative and non-radiative transitions in the SM. We conclude this study in SEC. IV.

#### II. METHOD OF CALCULATION

The optimized structure of BD1 in the ground state was obtained. The structure was confirmed to be the minimum energy structure using vibrational analysis. Excited adiabatic (AD) states were obtained by carrying out geometry optimizations and calculating the electronic states at the optimized structures. The normal modes were also obtained by vibrational analyses. Regarding the AD states, vibrational analyses were carried out for  $S_0$  at the optimized structures for the excited states. These calculations were performed at the B3LYP/6-311+G(d,p) and TD-B3LYP/6-311+G(d,p) levels of theory for the ground and excited states, respectively. In the excited state calculations, ten singlet and ten triplet states were taken into consideration. Off-diagonal VCCs between triplet states  $T_m-T_n$ , as well as singlet states  $S_m-S_n$  were calculated. VCD analyses were carried out for strong coupling modes. The electronic and vibrational states were calculated using Gaussian 09 Revision D.01[16], while the VCC calculations and VCD analyses were performed using our in-house codes.

#### III. RESULTS AND DISCUSSION

#### A. Franck-Condon Excited States

The symmetry of the optimized structure for the ground state is  $D_2$ . FC states were calculated at the optimized structure for  $S_0$ . FIG. 2 shows the energy levels of the FC states. The energy levels of  $T_3$  and  $T_4$  are close to those of  $S_2$ ,  $S_3$ , and  $S_4$ . Therefore, the

geometrical structures of T<sub>4</sub>, T<sub>3</sub>, S<sub>4</sub>, S<sub>3</sub>, S<sub>2</sub>, and S<sub>1</sub> were optimized.

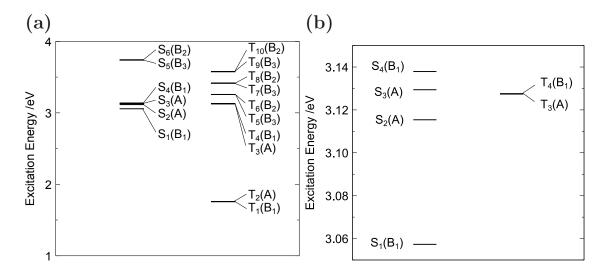


FIG. 2. (a) Energy levels of the excited states in BD1 at the optimized structure for  $S_0$ , and (b) an enlarged view of the relevant levels.

#### B. Optimized Structures of the Excited states

FIG. S1 in the SM[14] shows the optimized structures of the relevant excited states, i.e.  $T_3$ ,  $T_4$ ,  $S_2$ , and  $S_1$  as well as  $S_0$ . All the optimized structures show  $D_2$  symmetry. The dihedral angles (C1–C2–C3–C4) between the anthracene and benzene moieties (see FIG. 1) for the optimized structures are shown in S2. The dihedral angles of  $S_0$  and  $S_4$  are close to the right angle, while those of  $T_3$ ,  $T_4$ , and  $S_1$  are small.

## C. Frontier Orbitals

Frontier orbitals and their energy levels at the optimized structure of the ground state are shown in FIGs. 3 and 4. The NHOMO  $\psi_{\text{NHO}}$  and HOMO  $\psi_{\text{HO}}$  as well as the NLUMO  $\psi_{\text{NLU}}$  and LUMO  $\psi_{\text{LU}}$  are pseudo-degenerate. From FIG. 3, the frontier orbitals can be approximately represented as follows:

$$\psi_{\text{LU}} \approx \frac{1}{\sqrt{2}} (\phi_{\text{LU}}(L) - \phi_{\text{LU}}(R)), \quad \psi_{\text{NLU}} \approx \frac{1}{\sqrt{2}} (\phi_{\text{LU}}(L) + \phi_{\text{LU}}(R)), \quad (11)$$

$$\psi_{\text{HO}} \approx \frac{1}{\sqrt{2}} (\phi_{\text{HO}}(L) + \phi_{\text{HO}}(R)), \quad \psi_{\text{NHO}} \approx \frac{1}{\sqrt{2}} (\phi_{\text{HO}}(L) - \phi_{\text{HO}}(R)), \tag{12}$$

where  $\phi_{\text{HO/LU}}(L/R)$  denotes the fragment MOs consisting of the HOMO/LUMO of the anthracene moiety Left(L)/Right(R).

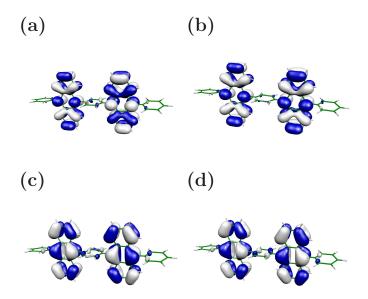


FIG. 3. Frontier orbitals of BD1: (a)  $B_2$  LUMO, (b)  $B_3$  NLUMO, (c)  $B_3$  HOMO, and (d)  $B_2$  NHOMO. The isosurface value is  $2.0 \times 10^{-2}$  a.u.

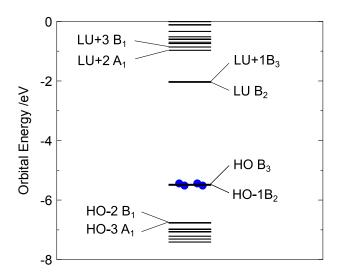


FIG. 4. Frontier orbital levels of BD1. It should be noted that the HOMO and next HOMO as well as the LUMO and next LUMO are pseudo-degenerate.

Since  $\phi_i(L)$  and  $\phi_j(R)$  are the fragment MOs,  $\phi_i(L)\phi_j(R) \approx 0$  (i, j = HO, NHO, LU, and)

NLU). Accordingly,

$$|\psi_{\rm LU}|^2 \approx |\psi_{\rm NLU}|^2 \tag{13}$$

$$\psi_{\rm HO}\psi_{\rm NLU} \approx \psi_{\rm NHO}\psi_{\rm LU}$$
 (14)

$$|\psi_{\rm HO}|^2 \approx |\psi_{\rm NHO}|^2 \tag{15}$$

$$\psi_{\text{HO}}\psi_{\text{LU}} \approx \psi_{\text{NHO}}\psi_{\text{NLU}}$$
 (16)

In addition,

$$\psi_{\text{HO}}\psi_{\text{NHO}} \neq \psi_{\text{LU}}\psi_{\text{NLU}}.$$
 (17)

In order to analyze VCDs and TDMDs obtained from the TD-DFT wave functions, these relations of the frontier orbitals will be used in SEC. III H.

#### D. Selection Rules

Since all the optimized structures show  $D_2$  symmetry, the selection rules for TDM, SOC, and vibronic coupling (VC) within  $D_2$  symmetry are discussed here. TABLE S1 in the SM[14] is the character table of the  $D_2$  point group. The direct products of the irreducible representations (irreps) are tabulated in TABLE S2. From TABLE S1, the components of the electric dipole operator,  $\hat{\mu}_x$ ,  $\hat{\mu}_y$ ,  $\hat{\mu}_z$  transform according to the  $B_3$ ,  $B_2$ , and  $B_1$  irreps, respectively, and the components of the orbital angular momentum operator,  $\hat{L}_x$ ,  $\hat{L}_y$ ,  $\hat{L}_z$  transform according to the  $B_3$ ,  $B_2$ , and  $B_1$  irreps, respectively. Based on TABLE S2, the selection rules for TDM, SOC, and VC were obtained and are listed in TABLEs S3, S4, and S5. According to TABLEs S3 and S4, an electric dipole transition or intersystem crossing between electronic states with the same irrep is symmetry forbidden.

TABLE S5 lists the selection rule for VC with  $D_2$  symmetry. The vibrational degrees of freedom in BD1 are decomposed into irreps as follows:

$$\Gamma_{vib} = 54a_1 \oplus 52b_1 \oplus 58b_2 \oplus 58b_3.$$
 (18)

According to TABLE S5, the number of vibronically active modes accounts for 1/4 of all the modes for every non-radiative transition  $m \to n$ . For example, in non-radiative transition  $S_1 \to S_0$ , the vibronically active modes are fifty two  $b_1$  modes because, as discussed later, the  $S_1$  state transforms as  $B_1$ .

#### E. Adiabatic Excited States

In this section, we discuss the excited states at their optimized geometries. The  $T_4$  state has lower energy than  $T_3$  at the  $T_n$  optimized structure (n = 3, 4), as shown in FIG. S3 in SEC. S5 of the SM[14]. Hereafter, we will refer to the electronic state at a certain geometry corresponding to the  $T_n$  state at the FC state as  $T_n$ .

FIG. 5 shows the energy levels of the excited states at the optimized structures for  $T_3$  and  $T_4$ . TABLE I lists the triplet excited states at the optimized structure for  $T_3$ . The irrep of  $T_3$  is A. Although  $T_3$  is close to  $S_2$  with  $\Delta E_{T_3-S_2}=0.8$  meV, RISC between  $T_3$  and  $S_2$  is symmetry forbidden. The electric dipole transition  $T_3 \to T_4$  and internal conversion (IC)  $T_3 \to T_4$  via  $b_1$  modes are allowed. These interactions are large because of a large overlap density between  $T_3$  and  $T_4$ , as discussed later. Therefore, a  $T_3$  exciton is immediately converted into a  $T_4$  exciton.

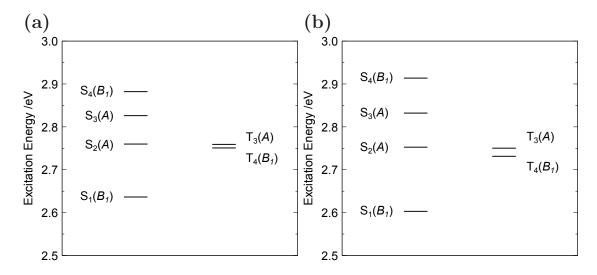


FIG. 5. Energy levels of excited states at the optimized structures for (a) T<sub>3</sub> and (b) T<sub>4</sub>.

TABLE II lists the triplet excited states at the optimized structure for  $T_4$ .  $T_4$  is close to  $S_2$  with  $\Delta E_{S_2-T_4}=21$  meV, and RISC between  $T_4$  and  $S_2$  is symmetry allowed because the  $T_4$  and  $S_2$  states belong to the  $B_1$  and A irreps, respectively. Although the electric dipole transition  $T_4 \to T_1$  is symmetry forbidden, that between  $T_4$  and  $T_2$  is symmetry allowed. In addition, IC  $T_4 \to T_2$  with the help of  $b_1$  modes and IC  $T_4 \to T_1$  with the help of a modes are symmetry allowed. However, the transitions  $T_4 \to T_2$  and  $T_4 \to T_1$  are suppressed because of small overlap densities of  $T_4$  with  $T_2$  and  $T_1$ , as discussed later. Therefore, a  $T_4$  exciton can be up-converted into an  $S_2$  exciton with thermal excitation. Accordingly, the

TABLE I. Triplet excited states at the optimized structure for  $T_3$ .

Excitation Energy Major Configuration						
	eV	nm	(CI Coefficient)			
$T_4(B_1)$	2.7508	450.72	$HO-1 \rightarrow LU+1 (0.524), HO \rightarrow LU (-0.455)$			
$T_3(A)$	2.7591	449.37	$HO-1 \rightarrow LU(-0.501), HO \rightarrow LU+1(0.496)$			
$T_2(A)$	1.4403	860.84	${\rm HO} {\rightarrow} {\rm LU} {+} 1 (0.502), {\rm HO} {-} 1 {\rightarrow} {\rm LU} (0.497)$			
$T_1(B_1)$	1.4252	869.93	${ m HO}{ ightarrow} { m LU}(\mbox{-}0.539), { m HO}{ m -}1{ ightarrow} { m LU}{ m +}1(\mbox{-}0.458)$			

 $T_3$  and  $T_4$  excitons generated via electrical excitation are up-converted into  $S_2$  excitons via RISC from the  $T_4$  state.

TABLE II. Triplet excited states at the optimized structure for  $T_4$ .

Excitation Energy Major Configuration						
$\mathrm{eV}$	nm	(CI coefficient)				
$T_3(A)$ 2.7503	450.81	$HO-1 \rightarrow LU(-0.501), HO \rightarrow LU+1(0.495)$				
$T_4(B_1) \ 2.7314$	453.93	$ \text{HO-1}{\rightarrow} \text{LU+1} (0.522), \\ \text{HO}{\rightarrow} \text{LU} (\text{-}0.436) $				
$T_2(A)$ 1.4590	849.77	${\rm HO}{\to}{\rm LU}{+}1(0.501), {\rm HO}{-}1{\to}{\rm LU}(0.495)$				
$T_1(B_1) \ 1.4345$	864.29	$HO \rightarrow LU(-0.549), HO-1 \rightarrow LU+1(-0.444)$				

FIG. 6 shows the energy levels of the excited states at the optimized structures for  $S_2$  and  $S_1$ . The singlet states at the optimized structure for  $S_2$  are tabulated in TABLE III. IC  $S_2 \to S_0$  via a modes and IC  $S_2 \to S_1$  via  $b_1$  modes are symmetry allowed. As we will show later, the transition probability of IC between  $S_2$  and  $S_0$  is small, while that between  $S_2$  and  $S_1$  is large. The electric dipole transition  $S_2 \to S_0$  is symmetry forbidden. On the other hand, the electric dipole transition  $S_2 \to S_1$  is symmetry allowed, and the TDM is thus large because of a large overlap density between  $S_2$  and  $S_1$ . Therefore, an  $S_2$  exciton is relaxed into the  $S_1$  state.

The singlet states at the optimized structure for  $S_1$  are listed in TABLE IV.  $S_1$  belongs to the  $B_1$  irrep and is the fluorescent state, as indicated by the oscillator strengths f listed in TABLE IV.

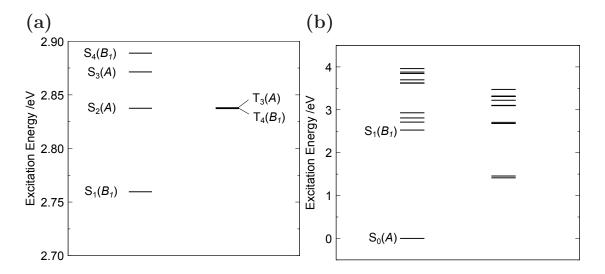


FIG. 6. Energy levels of the excited states at the optimized structures for (a)  $S_2$  and (b)  $S_1$ .

TABLE III. Singlet excited states at the optimized structure for  $S_2$ .

	Excitatio	n Energy		Major configuration
	${ m eV}$	nm	Osc.	(CI coefficient)
$S_4(B_1)$	2.8889	429.18	0.1041	$HO-1 \rightarrow LU+1 (0.698)$
$S_3(A)$	2.8714	431.80	0.0000	$\text{HO-1}{\rightarrow}\text{LU}(0.591), \text{HO}{\rightarrow}\text{LU}{+}1(0.379)$
$S_2(A)$	2.8375	436.95	0.0000	${\rm HO}{\to}{\rm LU}{+}1 (0.593), {\rm HO}{-}1{\to}{\rm LU} (\text{-}0.382)$
$S_1(B_1)$	2.7596	449.28	0.3131	$HO \rightarrow LU(0.698)$

TABLE IV. Singlet excited states at the optimized structure for  $S_1$ .

	Excitation	on Energy		Major configuration
	$\mathrm{eV}$	nm	Osc.	(CI coefficient)
$S_4(B_1)$	2.9295	423.23	0.0981	$HO-1 \rightarrow LU+1 (0.704)$
$S_3(A)$	2.8099	441.24	0.0000	$HO-1 \rightarrow LU(-0.546), HO \rightarrow LU+1(-0.442)$
$S_2(A)$	2.7124	457.09	0.0000	$HO \rightarrow LU+1 (0.547), HO-1 \rightarrow LU (-0.444)$
$S_1(B_1)$	2.5267	490.70	0.4800	$\mathrm{HO}{ ightarrow}\mathrm{LU}(\text{-}0.705)$

## F. Off-Diagonal Vibronic Coupling Constants

The calculated off-diagonal VCCs are shown in FIG. 7. Vibrational modes with strong couplings are shown in SEC. S6 of the SM[14]. From FIG. 7, the transition probabilities of

the ICs are in the following order:

$$T_3 \to T_4 > S_2 \to S_1 \gg S_1 \to S_0 \gg S_2 \to S_0 > T_4 \to T_1 > T_4 \to T_2.$$
 (19)

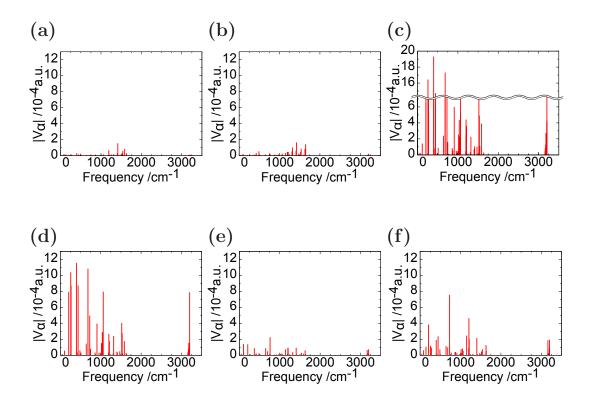


FIG. 7. Off-diagonal VCCs of (a)  $T_4@T_4 \rightarrow T_2@T_4$ , (b)  $T_4@T_4 \rightarrow T_1@T_4$ , (c)  $T_3@T_3 \rightarrow T_4@T_3$ , (d)  $S_2@S_2 \rightarrow S_1@S_2$ , (e)  $S_2@S_2 \rightarrow S_0@S_2$ , and (f)  $S_1@S_1 \rightarrow S_0@S_1$ .  $@T_n/@S_n$  denote the geometry used in optimization for the  $T_n/S_n$  state.

Based on the discussion in SEC. IIIE and Eq. 19, the scheme of excited state dynamics is depicted in FIG. 8. For the present FvHT mechanism, ICs such as  $S_2 \to S_0$ ,  $T_4 \to T_1$ , and  $T_4 \to T_2$  should be suppressed. From FIG. 7 and Eq. 19, the transition probabilities of these undesirable non-radiative processes are small. On the other hand, the non-radiative transition probabilities of the ICs  $S_2 \to S_1$  and  $T_3 \to T_4$  are large. In addition, electric dipole transition  $S_2 \to S_0$  and RISC  $T_3 \to S_2$  are symmetry forbidden. Therefore, the transitions  $S_2 \to S_1$  and  $T_3 \to T_4$  are preferable. A  $T_3$  exciton is converted into a  $T_4$  exciton to yield a  $S_2$  exciton via RISC, and the  $S_2$  exciton is then converted into a fluorescent  $S_1$  exciton. Accordingly, we can conclude that both  $T_3$  and  $T_4$  excitons are effectively converted into a fluorescent  $S_1$  exciton. It should also be noted that the transition probability of IC  $S_1 \to S_0$ 

is small enough for a  $S_1$  exciton to emit fluorescence.

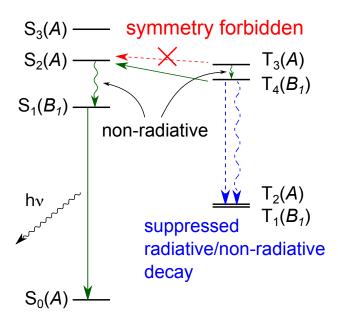


FIG. 8. Scheme of the excited state dynamics in BD1. Horizontal solid arrows indicate RISC, vertical straight arrows indicate radiative transitions, and wavy arrows denote non-radiative transitions.

#### G. Vibronic Coupling Density Analyses

In SEC. S7 of the SM[14], the VCD analyses for  $T_3$ – $T_4$ ,  $T_4$ – $T_2$ ,  $T_4$ – $T_1$ ,  $S_2$ – $S_1$ ,  $S_2$ – $S_0$ , and  $S_1$ – $S_0$  are shown. Note that the isosurface values are different. As was discussed in SEC. III F, the off-diagonal VCCs for  $T_3$ – $T_4$  and  $S_2$ – $S_1$  are large. As shown in FIGs. S10 and S13 in SEC. S7 of the SM[14], the VCDs for these VCs are localized on the anthracene moieties, which can be attributed to the large distributions of overlap densities on the anthracene moieties. On the other hand, the off-diagonal VCCs for  $T_4$ – $T_2$ ,  $T_4$ – $T_1$ , and  $S_2$ – $S_0$  are small. As shown in s S11, S12, and S14, the VCDs for these VCs are small, which is attributed to the disappearance of overlap densities. The mechanisms of disappearance are discussed in SEC. III H.

#### H. Overlap Densities

FIG. 9 shows the overlap densities having the same isosurface values. Among them, the overlap densities for  $T_4$ – $T_2$ ,  $T_4$ – $T_1$ , and  $S_2$ – $S_0$  disappear. In this section, we discuss the disappearance of these overlap densities.

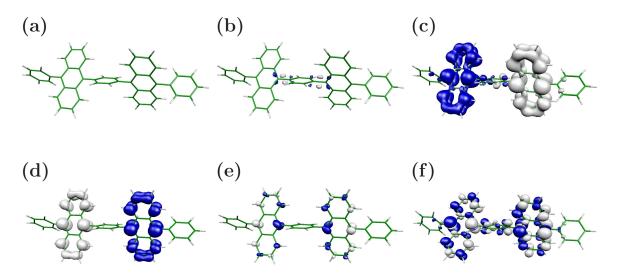


FIG. 9. Overlap densities for (a)  $T_4@T_4-T_2@T_4$ , (b)  $T_4@T_4-T_1@T_4$ , (c)  $T_3@T_3-T_4@T_3$ , (d)  $S_2@S_2-S_1@S_2$ , (e)  $S_2@S_2-S_0@S_2$ , and (f)  $S_1@S_1-S_0@S_1$ , respectively. All isosurface values are the same, i.e.  $1.0 \times 10^{-3}$  a.u.

A TD-DFT wave function is given by

$$\Psi_n = \sum_{i \in \text{occ}} \sum_{r \in \text{unocc}} C_i^r \Phi_i^r, \tag{20}$$

where  $\Phi_i^r$  represents the electronic configuration of a single-electron excitation from occupied orbital i to vacant orbital r, and  $C_i^r$  represents the CI coefficient.

The overlap density between two excited states  $\Psi_m$  and  $\Psi_n$ ,  $\rho^{mn}$ , is given by

$$\rho^{mn} = \sum_{i \in \text{occ}} \sum_{r \in \text{unocc}} \sum_{j \in \text{occ}} \sum_{s \in \text{unocc}} D_j^{s*} C_i^r \rho(\Phi_j^s, \Phi_i^r), \tag{21}$$

where  $D_j^s$  is the CI coefficient of another excited state m, and  $\rho(\Phi_j^s, \Phi_i^r)$  denotes the overlap density between the two configurations.

 $\Phi_0$  represents a ground state electron configuration, and its overlap density  $\rho_0$  is given by

$$\rho(\Phi_0, \Phi_0) =: \rho_0. \tag{22}$$

The overlap densities for various configurations are summarized as follows,

$$\rho(\Phi_i^r, \Phi_i^r) = \rho_0 - |\psi_i|^2 + |\psi_r|^2, \quad \rho(\Phi_0, \Phi_i^r) = \psi_i^* \psi_r, \quad \rho(\Phi_i^r, \Phi_i^r) = \psi_i^* \psi_j \quad (i \neq j), \tag{23}$$

$$\rho(\Phi_i^r, \Phi_i^s) = \psi_r^* \psi_s \quad (r \neq s), \quad \rho(\Phi_i^r, \Phi_i^s) = 0 \quad (i \neq j, r \neq s), \tag{24}$$

where  $\psi$  represents a molecular orbital.

According to TABLEs I, II, III, and IV, the approximate wave functions for the relevant excited states can be written as follows:

$$\Psi_a = C_1^a \Phi_{\text{HO}}^{\text{LU}} + C_2^a \Phi_{\text{NHO}}^{\text{NLU}}, \quad (T_4 @ T_4)$$
 (25)

$$\Psi_b = C_3^b \Phi_{\text{HO}}^{\text{NLU}} + C_4^b \Phi_{\text{NHO}}^{\text{LU}}, \quad (S_2@S_2)$$
 (26)

$$\Psi_c = C_1^c \Phi_{\text{HO}}^{\text{LU}} + C_2^c \Phi_{\text{NHO}}^{\text{NLU}}, \quad (T_1@T_4)$$
 (27)

$$\Psi_d = \Phi_{\rm HO}^{\rm LU}, \quad (S_1@S_2)$$
 (28)

$$\Psi_e = C_3^e \Phi_{\text{HO}}^{\text{NLU}} + C_4^e \Phi_{\text{NHO}}^{\text{LU}}, \quad (T_2@T_4)$$
 (29)

$$\Psi_0 = \Phi_0, \quad (S_0 @ S_2) \tag{30}$$

where the set of the CI coefficients is assumed to satisfy the following relation:

$$C_1^a \approx -C_2^a \approx C_3^b \approx -C_4^b \approx C_1^c \approx C_2^c \approx C_3^e \approx C_4^e \approx c. \tag{31}$$

In addition, we should recall the conditions of orbital overlap densities among the frontier orbitals discussed in SEC. III C. In general, these conditions for excited wave functions can be satisfied in systems with pseudo-degenerate excited electronic states.

In order to elucidate the reason for the disappearance of the overlap densities shown in FIG. 9, we discuss the overlap densities between approximate excited wave functions.

(Case 1:  $\Psi_a$  and  $\Psi_e$ ) This case corresponds to  $T_4$ – $T_2$ . The overlap density between  $\Psi_a$  and  $\Psi_e$  is given by

$$\rho^{ae} = (C_1^a C_3^e + C_2^a C_4^e) \psi_{\text{LU}} \psi_{\text{NLU}} + (C_1^a C_4^e + C_2^a C_3^e) \psi_{\text{HO}} \psi_{\text{NHO}}.$$
 (32)

From the condition for the CI coefficients (Eq. 31),

$$C_1^a C_3^e + C_2^a C_4^e \approx 0, \quad C_1^a C_4^e + C_2^a C_3^e \approx 0.$$
 (33)

Thus, the overlap density between  $\Psi_a$  and  $\Psi_e$  is cancelled out. Note that the disappearance of overlap density originates from the condition of the CI coefficients.

(Case 2:  $\Psi_a$  and  $\Psi_c$ ) This case corresponds to  $T_4$ – $T_1$ . The overlap density between  $\Psi_a$  and  $\Psi_c$  is given by

$$\rho^{ac} = C_1^a C_1^c \left( \rho_0 - |\psi_{\text{HO}}|^2 + |\psi_{\text{LU}}|^2 \right) + C_2^a C_2^c \left( \rho_0 - |\psi_{\text{NHO}}|^2 + |\psi_{\text{NLU}}|^2 \right). \tag{34}$$

From the condition for the CI coefficients,

$$\rho^{ac} \approx c^2 \left( |\psi_{\text{NHO}}|^2 - |\psi_{\text{HO}}|^2 + |\psi_{\text{LU}}|^2 - |\psi_{\text{NLU}}|^2 \right). \tag{35}$$

From the condition for the orbital densities, Eqs. 13 and 15

$$\rho^{ac} \approx 0. \tag{36}$$

Note that the disappearance of overlap density originates from the condition of the orbital densities of the frontier orbitals as well as that of the CI coefficients.

(Case 3:  $\Psi_b$  and  $\Psi_0$ ) This case corresponds to  $S_2$ – $S_0$ . The overlap density between  $\Psi_b$  and  $\Psi_0$  is given by

$$\rho^{b0} \approx c(\psi_{\rm HO}\psi_{\rm NLU} - \psi_{\rm NHO}\psi_{\rm LU}). \tag{37}$$

According to Eq. 14 and FIG. 10,  $\rho^{b0}$  is cancelled out. Note that the disappearance of overlap density originates from the condition of the orbital overlap densities of the frontier orbitals as well as that of the CI coefficients.

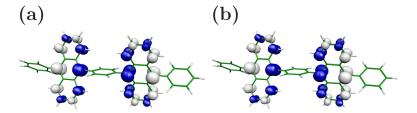


FIG. 10. Orbital overlap densities, (a)  $\psi_{\text{HO}}\psi_{\text{NLU}}$  and (b)  $\psi_{\text{NHO}}\psi_{\text{LU}}$ , at the optimized structure for S<sub>2</sub>. The isosurface value is  $1.0 \times 10^{-3}$  a.u.

(Case 4:  $\Psi_b$  and  $\Psi_d$ ) This case corresponds to  $S_2$ – $S_1$ . According to Eq. 17, the overlap density between  $\Psi_b$  and  $\Psi_d$  is given by

$$\rho^{bd} \approx c(\psi_{\text{NLU}}\psi_{\text{LU}} - \psi_{\text{NHO}}\psi_{\text{HO}}) \neq 0.$$
 (38)

Thus,  $\rho^{bd}$  is not cancelled out.

General cases are discussed in SEC. S8 of the SM[14].

These reduced overlap densities, which originate from the pseudo degeneracy, are responsible for the suppression of undesirable radiative and non-radiative transitions,  $T_3 \to T_2$ ,  $T_3 \to T_1$ , and  $S_2 \to S_0$ , for the FvHT mechanism because TDM and VCC depend on overlap density.

#### IV. CONCLUSION

To elucidate the high EQE observed in OLEDs using BD1, we calculated the off-diagonal VCCs and performed VCD analyses. The findings based on the calculations and analyses are as follows:

- 1. The large off-diagonal VCCs between  $T_3$ - $T_4$  cause the non-radiative transition from  $T_3$  to  $T_4$ .
- 2. As the overlap densities between  $T_4$ – $T_2$ / $T_4$ – $T_1$  are small, radiative/non-radiative processes are suppressed.
- 3. RISC from  $T_4$  to  $S_2$  is symmetry allowed and the energy gap between them is small  $(\Delta E_{S_2-T_4} = 21 \text{ meV}).$
- 4. Owing to the large overlap density between  $S_2$ – $S_1$ , radiative/non-radiative relaxation occurs from  $S_2$  to  $S_1$ , which results in emission from  $S_1$ .
- 5. The undesirable radiative/non-radiative transitions can be suppressed by utilizing the pseudo-degeneracy. Therefore, RISC via  $T_4$  can be the dominant pathway.

We employed the overlap densities calculated from N-electron wave functions to take the multi-configurational property of the excited states into consideration. This property cannot be captured using only a transition density (orbital overlap density).

We proposed a fluorescence via higher triplets (FvHT) emitting mechanism for OLEDs based on a bisanthracene derivative, BD1. This mechanism is valid as long as all transitions from  $T_m$  (m > 1) to all lower  $T_n$  ( $m > n \ge 1$ ) are suppressed. In BD1, we found that this condition is satisfied because of its pseudo-degenerate electronic structure. The excited electronic structure of BD1 is different from that of PTZ-BZP in which the LUMO and NLUMO are pseudo-degenerate, but the HOMO and NHOMO are not. We also discussed

the general conditions for the disappearance of the overlap densities in the pseudo-degenerate system. The general conditions are applicable not only for transitions in a molecule, but also for exciton migrations in the solid phase.

The concepts of iST and SC-TADF are based on the selection rules for a molecular symmetry group. In contrast, the design principle based on the FvHT mechanism allows the use of asymmetric molecules. In fact, the molecular structure of BD1 shows  $D_2$  symmetry and is thus not suitable as an iST nor SC-TADF molecule, as expressed in Eq. 2. (If the dihedral angle of BD1 were to be the right angle, BD1 could show  $D_{2h}$  symmetry and exhibit iST or SC-TADF. See SEC. S9 of the SM[14].)

Finally, we propose a superordinate concept, fluorescence via RISC (FvRISC) from T<sub>1</sub> or higher triplet states. This concept includes TADF, SC-TADF, iST, and FvHT. The concept of FvRISC enables us to overcome the singlet exciton formation ratio of 25 % for electrical excitations and to realize highly efficient OLEDs.

#### ACKNOWLEDGMENTS

We thank Prof. Hirofumi Sato. Numerical calculations were partly performed at the Supercomputer Laboratory of Kyoto University and at the Research Center for Computational Science, Okazaki, Japan. This study was also supported by a Grant-in-Aid for Scientific Research (C) (15K05607) from the Japan Society for the Promotion of Science (JSPS).

<sup>[1]</sup> Chihaya Adachi, "Third-generation organic electroluminescence materials," Jpn. J. Appl. Phys. **53**, 060101 (2014).

<sup>[2]</sup> Ayataka Endo, Mai Ogasawara, Atsushi Takahashi, Daisuke Yokoyama, Yoshimine Kato, and Chihaya Adachi, "Thermally activated delayed fluorescence from Sn<sup>4+</sup>-porphyrin complexes and their application to organic light emitting diodes – a novel mechanism for electroluminescence," Adv. Mater. **21**, 4802–4806 (2009).

<sup>[3]</sup> Hiroyuki Tanaka, Katsuyuki Shizu, Hiroshi Miyazaki, and Chihaya Adachi, "Efficient green thermally activated delayed fluorescence (TADF) from a phenoxazine-triphenyltriazine (PXZ-TRZ) derivative," Chem. Commun. 48, 11392–11394 (2012).

- [4] Hiroki Uoyama, Kenichi Goushi, Katsuyuki Shizu, Hiroko Nomura, and Chihaya Adachi, "Highly efficient organic light-emitting diodes from delayed fluorescence," Nature 492, 234–238 (2012).
- [5] Sae Youn Lee, Takuma Yasuda, Hiroko Nomura, and Chihaya Adachi, "High-efficiency organic light-emitting diodes utilizing thermally activated delayed fluorescence from triazine-based donor-acceptor hybrid molecules," Appl. Phys. Lett. 101, 093306 (2012).
- [6] Tetsuya Nakagawa, Sung-Yu Ku, Ken-Tsung Wong, and Chihaya Adachi, "Electroluminescence based on thermally activated delayed fluorescence generated by a spirobifluorene donor-acceptor structure," Chem. Commun. 48, 9580–9582 (2012).
- [7] Gábor Méhes, Hiroko Nomura, Qisheng Zhang, Tetsuya Nakagawa, and Chihaya Adachi, "Enhanced electroluminescence efficiency in a spiro-acridine derivative through thermally activated delayed fluorescence," Angew. Chem., Int. Ed. **51**, 11311–11315 (2012).
- [8] Hironori Kaji, Hajime Suzuki, Tatsuya Fukushima, Katsuyuki Shizu, Katsuaki Suzuki, Shosei Kubo, Takeshi Komino, Hajime Oiwa, Furitsu Suzuki, Atsushi Wakamiya, Yasujiro Murata, and Chihaya Adachi, "Purely organic electroluminescent material realizing 100% conversion from electricity to light," Nat. Commun. 6, 8476 (2015).
- [9] Tohru Sato, Motoyuki Uejima, Naoya Iwahara, Naoki Haruta, Katsuyuki Shizu, and Kazuyoshi Tanaka, "Vibronic coupling density and related concepts," J. Phys.: Conf. Ser. 428, 012010 1–19 (2013).
- [10] Motoyuki Uejima, Tohru Sato, Daisuke Yokoyama, Kazuyoshi Tanaka, and Jong-Wook Park, "Quantum yield in blue-emitting anthracene derivatives: vibronic coupling density and transition dipole moment density," Phys. Chem. Chem. Phys. 16, 14244–14256 (2014).
- [11] Tohru Sato, Motoyuki Uejima, Kazuyoshi Tanaka, Hironori Kaji, and Chihaya Adachi, "A light-emitting mechanism for organic light-emitting diodes: molecular design for inverted singlet-triplet structure and symmetry-controlled thermally activated delayed fluorescence,"
  J. Mater. Chem. C 3, 870–878 (2015).
- [12] Liang Yao, Shitong Zhang, Rong Wang, Weijun Li, Fangzhong Shen, Bing Yang, and Yuguang Ma, "Highly efficient near-infrared organic light-emitting diode based on a butterfly-shaped donor-acceptor chromophore with strong solid-state fluorescence and a large proportion of radiative excitons," Angew. Chem., Int. Ed. 126, 2151–2155 (2014).

- [13] Tohru Sato, "Fluorescence via reverse intersystem crossing from higher triplet states," J. Comput. Chem., Jpn. 14, 189–192 (2015).
- [14] See Supplemental Material for radiative and non-radiative transition rates; vibronic coupling density and transition dipole moment density; optimized structures of BD1; selection rules for  $D_2$ ; energy shifts of the triplet excited states during optimizations; vibrational modes with strong couplings; vibronic coupling density analyses; general conditions for the disappearance of overlap densities in pseudo-degenerate systems; and imposition of the  $D_{2h}$ -symmetry constraint on BD1.
- [15] Jian-Yong Hu, Yong-Jin Pu, Fumiya Satoh, So Kawata, Hiroshi Katagiri, Hisahiro Sasabe, and Junji Kido, "Bisanthracene-based donor-acceptor-type light-emitting dopants: Highly efficient deep-blue emission in organic light-emitting devices," Adv. Funct. Mater. 24, 2064–2071 (2014).
- [16] M. J. Frisch, G. W. Trucks, H. B. Schlegel, G. E. Scuseria, M. A. Robb, J. R. Cheeseman, G. Scalmani, V. Barone, B. Mennucci, G. A. Petersson, H. Nakatsuji, M. Caricato, X. Li, H. P. Hratchian, A. F. Izmaylov, J. Bloino, G. Zheng, J. L. Sonnenberg, M. Hada, M. Ehara, K. Toyota, R. Fukuda, J. Hasegawa, M. Ishida, T. Nakajima, Y. Honda, O. Kitao, H. Nakai, T. Vreven, J. A. Montgomery, Jr., J. E. Peralta, F. Ogliaro, M. Bearpark, J. J. Heyd, E. Brothers, K. N. Kudin, V. N. Staroverov, R. Kobayashi, J. Normand, K. Raghavachari, A. Rendell, J. C. Burant, S. S. Iyengar, J. Tomasi, M. Cossi, N. Rega, J. M. Millam, M. Klene, J. E. Knox, J. B. Cross, V. Bakken, C. Adamo, J. Jaramillo, R. Gomperts, R. E. Stratmann, O. Yazyev, A. J. Austin, R. Cammi, C. Pomelli, J. W. Ochterski, R. L. Martin, K. Morokuma, V. G. Zakrzewski, G. A. Voth, P. Salvador, J. J. Dannenberg, S. Dapprich, A. D. Daniels, . Farkas, J. B. Foresman, J. V. Ortiz, J. Cioslowski, and D. J. Fox, "Gaussian 09 revision D.01," Gaussian Inc. Wallingford CT 2009.

## **Supplemental Material**

# Fluorescence via Reverse Intersystem Crossing from Higher Triplet States in a Bisanthracene Derivative

Tohru Sato,\*a,b Rika Hayashic, Naoki Harutaa, and Yong-Jin Pud,e

September 21, 2016

<sup>&</sup>lt;sup>a</sup> Department of Molecular Engineering, Graduate School of Engineering, Kyoto University, Nishikyo-ku, Kyoto 615-8510, Japan; Tel: +81-75-383-2544; Fax: +81-75-383-2799; E-mail: tsato@moleng.kyoto-u.ac.jp

<sup>&</sup>lt;sup>b</sup> Unit of Elements Strategy Initiative for Catalysts & Batteries, Kyoto University, Nishikyo-ku, Kyoto 615-8510, Japan

<sup>&</sup>lt;sup>c</sup> Undergraduate School of Industrial Chemistry, Faculty of Engineering, Kyoto University, Nishikyo-ku, Kyoto 615-8510, Japan

<sup>&</sup>lt;sup>d</sup> Department of Organic Device Engineering and Research Center for Organic Electronics, Yamagata University, 4-3-16, Johnan, Yonezawa, 992-8510, Japan

<sup>&</sup>lt;sup>e</sup> PRESTO (Sakigake), JST

## **Contents**

<b>S</b> 1	Radi	ative and Non-Radiative Transition Rates	83
S2	Vibro	onic Coupling Density and Transition Dipole Moment Density	<b>S4</b>
S3	Opti	mized Structures	S5
S4	Selec	tion Rules	<b>S6</b>
S5	Leve	Shifts of Triplet Excites States during Optimizations	<b>S8</b>
S6	Vibra	ational Modes with Strong Couplings	<b>S9</b>
<b>S7</b>	Vibro	onic Coupling Density Analyses	S10
S8	Gene	eral Conditions for Disappearances of Overlap Densities in Pseudo-Degenerate Systems	S11
<b>S9</b>	Impo	osition of $D_{2h}$ -Symmetry Constraint on BD1	S13
	<b>S</b> 1	Singlet and Triplet Excited States	S13
	S2	Subduction from $D_{2h}$ to $D_2$	S14

## S1 Radiative and Non-Radiative Transition Rates

We consider transition from the initial vibronic state  $|\Phi_{mi}\rangle = |\Psi_m\rangle |\chi_i\rangle$  to the final one  $|\Phi_{nj}\rangle = |\Psi_n\rangle |\chi_j\rangle$ , where  $|\Psi_m\rangle$  and  $|\chi_i\rangle$  denote the initial electronic and vibrational states, and  $|\Psi_n\rangle$  and  $|\chi_j\rangle$  stand for the final electronic and vibrational states, respectively. Radiative and non-radiative transition rate constants between these vibronic states can be obtained as per the Fermi's golden rule, which describes a transition rate constant between quantum states in a general manner, as described in our previous papers <sup>1,2</sup>. Summing radiative transition rate constants over all the vibrational states, the radiative transition rate constant  $k_r$  from the initial electronic state  $|\Psi_m\rangle$  to the final one  $|\Psi_n\rangle$  is given by

$$k_r = \int_0^\infty d\omega \frac{4\omega^3}{3c^3} \sum_{i,j} P_{mi}(T) |\boldsymbol{\mu}_{mn}|^2 |\langle \chi_{mi} | \chi_{nj} \rangle|^2 \delta(\hbar\omega - E_{mi} + E_{nj}), \tag{S1}$$

where  $\omega$  denotes an angular frequency of an emitted photon, c is the speed of light,  $P_{mi}(T)$  stands for the statistical weight of  $|\Phi_{mi}\rangle$  at the temperature T,  $\mu_{nm}$  is the transition dipole moment between  $|\Psi_{m}\rangle$  and  $|\Psi_{n}\rangle$ , and  $\hbar$  is the reduced Planck Constant. On the other hand, the non-radiative transition rate constant  $k_{nr,\alpha}$  via mode  $\alpha$  is given by

$$k_{nr,\alpha} = \frac{2\pi}{\hbar} \sum_{i,j} P_{mi}(T) |V_{mn,\alpha}|^2 |\langle \chi_{mi} | Q_{\alpha} | \chi_{nj} \rangle|^2 \delta(E_{mi} - E_{nj}), \tag{S2}$$

where  $V_{\alpha}^{mn}$  is the off-diagonal vibronic coupling constant between  $|\Psi_m\rangle$  and  $|\Psi_n\rangle$  with respect to mode  $\alpha$ , and  $Q_{\alpha}$  denotes a mass-weighted normal coordinate of mode  $\alpha$ .

## S2 Vibronic Coupling Density and Transition Dipole Moment Density

Suppose that an operator  $\hat{O}$  consists of one-electron operators  $\hat{o}$  without any differential operators,

$$\hat{O} = \sum_{i=1}^{N} \hat{o}(\mathbf{r}_i),\tag{S3}$$

where  $\mathbf{r}_i$  denotes the spatial coordinate of electron i. A matrix element of  $\hat{O}$  is given by <sup>1</sup>

$$O_{mn} = \int \cdots \int \Psi_{m}^{*} \hat{O} \Psi_{n} d^{4} \mathbf{x}_{1} \cdots d^{4} \mathbf{x}_{N}$$

$$= \sum_{i=1}^{N} \int \left[ \int \cdots \int \Psi_{m}^{*} \Psi_{n} d^{4} \mathbf{x}_{1} \cdots d^{4} \mathbf{x}_{i-1} ds_{i} d^{4} \mathbf{x}_{i+1} \cdots d^{4} \mathbf{x}_{N} \right] \hat{o}(\mathbf{r}_{i}) d^{3} \mathbf{r}_{i}$$

$$= \sum_{i=1}^{N} \int \left[ \frac{1}{N} \rho^{mn}(\mathbf{r}_{i}) \right] \hat{o}(\mathbf{r}_{i}) d^{3} \mathbf{r}_{i}$$

$$= \int \rho^{mn}(\mathbf{r}) \hat{o}(\mathbf{r}) d^{3} \mathbf{r}, \qquad (S4)$$

where  $\mathbf{x}_i = (\mathbf{r}_i, s_i)$  with spatial coordinate  $\mathbf{r}_i$  and spin coordinate  $s_i$  for electron i.  $\rho^{mn}(\mathbf{r}) \times \hat{o}(\mathbf{r})$  is a density form of the matrix element  $O_{mn}$ . It should be noted that any approximation is not employed in this derivation.

An electric dipole moment operator  $\hat{\mu}$  is an example of  $\hat{O}$ :

$$\hat{\boldsymbol{\mu}} := \sum_{i=1}^{N} -e\boldsymbol{r}_{i}. \tag{S5}$$

Therefore, a transition dipole moment  $\mu_{mn}$  between electronic states m and n is given by the integral of a transition dipole moment density  $\tau_{mn}(r) = \rho^{mn}(r) \times (-er)^{1,2}$ .

An off-diagonal vibronic coupling constant  $V_{\alpha}^{mn}$  is

$$V_{\alpha}^{mn} = \int \cdots \int \Psi_{m}^{*} \left(\frac{\partial U_{ne}}{\partial Q_{\alpha}}\right)_{\mathbf{R}_{0}} \Psi_{n} d^{4} \mathbf{x}_{1} \cdots d^{4} \mathbf{x}_{N} + \int \cdots \int \Psi_{m}^{*} \left(\frac{\partial U_{nn}}{\partial Q_{\alpha}}\right)_{\mathbf{R}_{0}} \Psi_{n} d^{4} \mathbf{x}_{1} \cdots d^{4} \mathbf{x}_{N}$$

$$= \int \cdots \int \Psi_{m}^{*} \left(\frac{\partial U_{ne}}{\partial Q_{\alpha}}\right)_{\mathbf{R}_{0}} \Psi_{n} d^{4} \mathbf{x}_{1} \cdots d^{4} \mathbf{x}_{N}, \tag{S6}$$

where  $U_{ne}$  denotes the sum of nuclear-electronic potentials,  $U_{nn}$  stands for the sum of nuclear-nuclear potentials, and  $Q_{\alpha}$  is a mass-weighted normal coordinate of mode  $\alpha$ . Since  $(\partial U_{ne}/\partial Q_{\alpha})_{R_0}$  can be written as the sum of one-electron potential derivatives:

$$\left(\frac{\partial U_{ne}}{\partial Q_{\alpha}}\right)_{\mathbf{R}_{0}} = \sum_{i=1}^{N} v_{\alpha}(\mathbf{r}_{i}),\tag{S7}$$

 $V_{\alpha}^{mn}$  is given by the integral of a vibronic coupling density  $\eta_{\alpha}^{mn}(\mathbf{r}) = \rho^{mn}(\mathbf{r}) \times v_{\alpha}(\mathbf{r})^{1,2}$ .

## S3 Optimized Structures

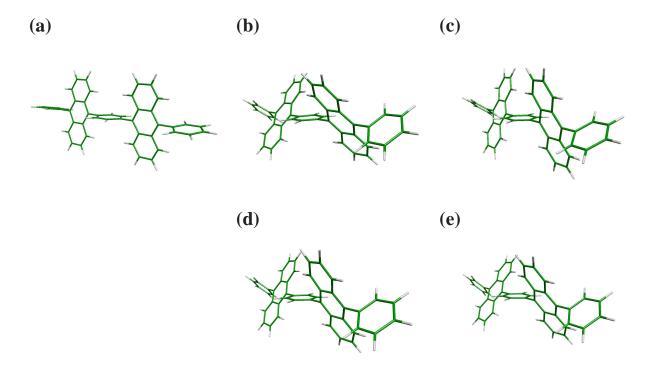


FIG. S1: Optimized structures of BD1 for (a)  $S_0$ , (b)  $S_1$ , (c)  $S_2$ , (d)  $T_3$ , and (e)  $T_4$ .

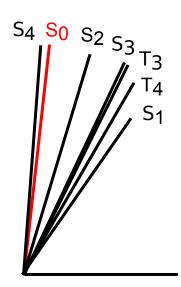


FIG. S2: Dihedral angles (C1–C2–C3–C4) between the anthracene and benzene moieties for the geometry-optimized excited states.

## **S4** Selection Rules

TABLE S1: Character table of  $D_2$ .

$D_2$	E	$C_2(z)$	$C_2(y)$	$C_2(x)$	h	a = 4
$A_1$	1	1	1	1		$x^2,y^2,z^2$
$B_1$	1	1	-1	-1	$z,R_z$	xy
$B_2$	1	-1	1	-1	$y,R_y$	zx
$B_3$	1	-1	-1	1	$x,R_x$	yz

TABLE S2: Direct products of irreducible representations in  $D_2$ .

$D_2$	$A_1$	$B_1$	$B_2$	$B_3$
$A_1$	$A_1$	$B_1$	$B_2$	$B_3$
$B_1$		$A_1$	$B_3$	$B_2$
$B_2$			$A_1$	$B_1$
$B_3$				$A_1$

TABLE S3: Selection rule of the transition dipole moment in  $D_2$ . — denotes a forbidden transition, and  $\mu_i$  (i = x, y, z) denotes a symmetry-allowed component of transition dipole moment  $\langle m|\hat{\mu}|n\rangle$ .

<i>m</i> / <i>n</i>	$A_1$	$B_1$	$B_2$	$B_3$
$A_1$	_	$\mu_z$	$\mu_y$	$\mu_x$
$B_1$		_	$\mu_x$	$\mu_y$
$B_2$			_	$\mu_z$
$B_3$				_

TABLE S4: Selection rule of spin-orbit coupling in  $D_2$ . — denotes a forbidden transition, and  $L_i$  (i = x, y, z) denotes a symmetry-allowed component of orbital angular moment  $\langle m|\hat{L}|n\rangle$ .

m/ n	$A_1$	$B_1$	$B_2$	$B_3$
$A_1$	_	$L_z$	$L_{y}$	$L_{x}$
$B_1$		_	$L_x$	$L_{y}$
$B_2$			_	$L_z$
$B_3$				_

TABLE S5: Selection rule of vibronic coupling in  $D_2$ . — denotes a forbidden transition, and  $V_{\Gamma}$  ( $\Gamma = A_1, B_1, B_2, B_3$ ) denotes a symmetry-allowed component of vibronic coupling constant  $\langle m|\hat{V}_{\Gamma}|n\rangle$ , where  $\hat{V}_{\Gamma} = (\partial H/\partial Q_{\Gamma})$  with normal coordinate  $Q_{\Gamma}$ .

m/ n	$A_1$	$B_1$	$B_2$	$B_3$
$A_1$	$V_{a_1}$	$V_{b_1}$	$V_{b_2}$	$V_{b_3}$
$B_1$		$V_{a_1}$	$V_{b_3}$	$V_{b_2}$
$B_2$			$V_{a_1}$	$V_{b_1}$
$B_3$				$V_{a_1}$

## S5 Level Shifts of Triplet Excites States during Optimizations

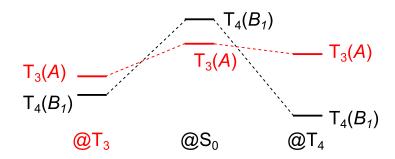


FIG. S3: Level shifts of triplet excited states of BD1 during geometry optimizations.

## **S6** Vibrational Modes with Strong Couplings

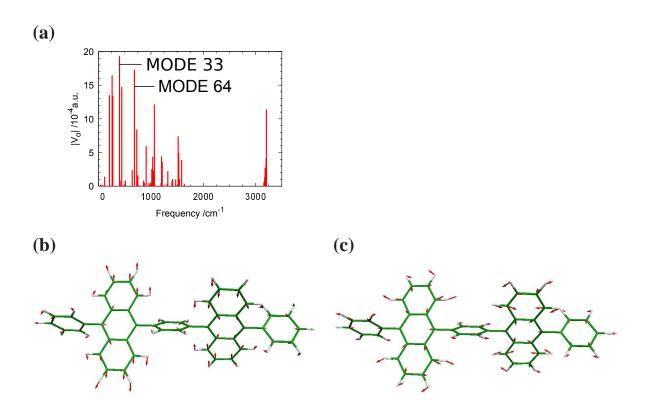


FIG. S4: (a) Off-diagonal VCCs between  $T_3$  and  $T_4$  at the  $T_3$  optimized structure, and strong coupling modes: (b) mode 33 and (c) mode 64.

## **S7** Vibronic Coupling Density Analyses

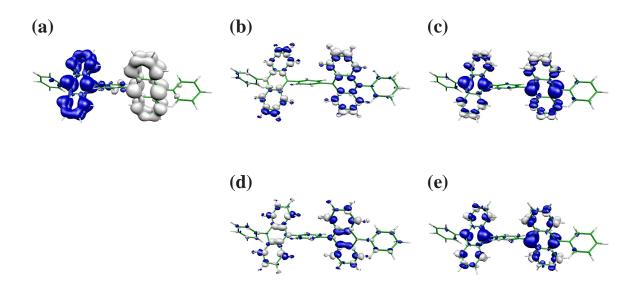


FIG. S5: Off-diagonal VCD analyses between  $T_3$  and  $T_4$  at the  $T_3$  optimized structure: (a) overlap density  $\rho_{34}$ , (b) potential derivative  $\nu_{33}$ , (c) VCD  $\eta_{34,33}$ , (d) potential derivative  $\nu_{64}$ , and (e) VCD  $\eta_{34,64}$ . The isosurface values for  $\rho$ ,  $\nu$ , and  $\eta$  are  $1.0 \times 10^{-3}$ ,  $5.0 \times 10^{-3}$  and  $5.0 \times 10^{-6}$  a.u., respectively.

## S8 General Conditions for Disappearances of Overlap Densities in Pseudo-Degenerate Systems

In this section, we discuss the overlap densities in a pseudo-degenerate system, (moiety L)-(linker)-(moiety R) system, in general, where moiety L and moiety R are the same fragments. As the pseudo-degenerate frontier orbitals, we consider the following forms:

$$\psi_{\text{LU}} = \frac{1}{\sqrt{2}} (\phi_{\text{LU}}(L) - \phi_{\text{LU}}(R)), \qquad \psi_{\text{NLU}} = \frac{1}{\sqrt{2}} (\phi_{\text{LU}}(L) + \phi_{\text{LU}}(R)), \tag{S8}$$

$$\psi_{\text{HO}} = \frac{1}{\sqrt{2}} (\phi_{\text{HO}}(L) + \phi_{\text{HO}}(R)), \qquad \psi_{\text{NHO}} = \frac{1}{\sqrt{2}} (\phi_{\text{HO}}(L) - \phi_{\text{HO}}(R)), \tag{S9}$$

where  $\phi_{\text{HO/LU}}(L/R)$  denotes a fragment HOMO/LUMO on moiety Left(L)/Right(R).

Since these frontier orbitals are localized on moieties L and R, the overlaps between the different moieties can be neglected:  $\phi_i(L)\phi_j(R) = 0$  (i, j =HO, NHO, LU, and NLU). Therefore, we can obtain the following relations of orbital overlap densities:

$$|\psi_{LU}|^2 = \frac{1}{2}(|\phi_{LU}(L)|^2 + |\phi_{LU}(R)|^2) = |\psi_{NLU}|^2 =: r,$$
 (S10)

$$\psi_{\text{HO}}\psi_{\text{NLU}} = \frac{1}{2}(\phi_{\text{LU}}(L)\phi_{\text{HO}}(L) + \phi_{\text{LU}}(R)\phi_{\text{HO}}(R)) = \psi_{\text{NHO}}\psi_{\text{LU}} =: s,$$
(S11)

$$|\psi_{\text{HO}}|^2 = \frac{1}{2}(|\phi_{\text{HO}}(L)|^2 + |\phi_{\text{HO}}(R)|^2) = |\psi_{\text{NHO}}|^2 =: t,$$
 (S12)

$$\psi_{\text{HO}}\psi_{\text{LU}} = \frac{1}{2}(\phi_{\text{LU}}(L)\phi_{\text{HO}}(L) - \phi_{\text{LU}}(R)\phi_{\text{HO}}(R)) = \psi_{\text{NHO}}\psi_{\text{NLU}} =: u.$$
(S13)

In addition, we define the orbital overlap densities

$$q := \psi_{\text{HO}} \psi_{\text{NHO}} = \frac{1}{2} (|\phi_{\text{HO}}(L)|^2 - |\phi_{\text{HO}}(R)|^2), \tag{S14}$$

$$p := \psi_{LU}\psi_{NLU} = \frac{1}{2}(|\phi_{LU}(L)|^2 - |\phi_{LU}(R)|^2). \tag{S15}$$

We consider wave functions of the pseudo-degenerate system shown in TABLE S6. The overlap densities of the pseudo-degenerate system are summarized in TABLE S7. The pairs denoted by 0 in TABLE S7 indicate reduced overlap density, i.e. suppressed radiative/non-radiative transition. This approach can be extended for degenerate systems and pseudo-degenerate systems with more than three-fold degeneracy.

TABLE S6: Approximate wave functions of a pseudo-degenerate system,  $c = 1/\sqrt{2}$ .

Approximate form of wave function	$@T_4/@T_3$	$@S_2/@S_1$
$\Psi_a = c\Phi_{\text{HO}}^{\text{LU}} - c\Phi_{\text{NHO}}^{\text{NLU}}$	$T_4$	
$\Psi_b = c\Phi_{\rm HO}^{\rm NLU} - c\Phi_{\rm NHO}^{\rm LU}$	$T_3$	$S_2$
$\Psi_c = c\Phi_{\text{HO}}^{\text{LU}} + c\Phi_{\text{NHO}}^{\text{NLU}}$	$T_1$	
$\Psi_d = \Phi^{ m LU}_{ m HO}$		$S_1$
$\Psi_e = c\Phi_{\rm HO}^{\rm NLU} + c\Phi_{\rm NHO}^{\rm LU}$	$T_2$	$S_3$
$\Psi_f = \Phi_{ m HO}^{ m NLU}$		
$\Psi_g = \Phi_{ m NHO}^{ m NLU}$		$S_4$
$\Psi_h = \Phi_{ m NHO}^{ m LU}$		
$\Psi_0 = \Phi_0$		$S_0$

TABLE S7: Overlage densities in a pseudo-degenerate system.  $\alpha = p - q$ ,  $\beta = \rho_0 - t + r$ , and  $\gamma = p + q$ .

	$\Psi_a$	$\Psi_b$	$\Psi_c$	$\Psi_d$	$\Psi_e$	$\Psi_f$	$\Psi_g$	$\Psi_h$	$\Psi_0$
$\Psi_a$		α	0	$c\beta$	0	cα	$-c\beta$	$-c\alpha$	0
$\Psi_b$			0	$c\alpha$	0	$c\beta$	$-c\alpha$	$-c\beta$	0
$\Psi_c$				$c\beta$	γ	$c\gamma$	$c\beta$	$c\gamma$	2cu
$\Psi_d$					$c\gamma$	p	0	q	и
$\Psi_e$						$c\beta$	$c\gamma$	$c\beta$	2cs
$\Psi_f$							q	0	S
$\Psi_g$								p	и
$\Psi_h$									S
$\Psi_0$									

## S9 Imposition of $D_{2h}$ -Symmetry Constraint on BD1

## S1 Singlet and Triplet Excited States

TABLE S8: Excited states of BD1 at the optimized structure for  $S_0$  with a  $D_{2h}$ -symmetry constraint.

State		Excitation Energy		Oscillator Strength
		eV	nm	
$T_1$	$^{3}B_{3u}$	2.2072	561.72	0.0000
$T_2$	$^{3}A_{g}$	2.2078	561.57	0.0000
$S_1$	$^{1}B_{3u}$	3.5520	349.05	0.5269
$S_2$	$^{1}A_{g}$	3.6186	342.63	0.0000
$T_3$	$^{3}B_{1g}$	3.7529	330.37	0.0000
T <sub>4</sub>	$^{3}B_{2u}$	3.7533	330.34	0.0000

## **S2** Subduction from $D_{2h}$ to $D_2$

$$A_g \downarrow D_2 = A \tag{S16}$$

$$B_{1g} \downarrow D_2 = B_1 \tag{S17}$$

$$B_{2g} \downarrow D_2 = B_2 \tag{S18}$$

$$B_{3g} \downarrow D_2 = B_3 \tag{S19}$$

$$A_u \downarrow D_2 = A \tag{S20}$$

$$B_{1u} \downarrow D_2 = B_1 \tag{S21}$$

$$B_{2u} \downarrow D_2 = B_2 \tag{S22}$$

$$B_{3u} \downarrow D_2 = B_3 \tag{S23}$$

## References

- 1 T. Sato, M. Uejima, N. Iwahara, N. Haruta, K. Shizu and K. Tanaka, *J. Phys.: Conf. Ser.*, 2013, **428**, 012010 1–19.
- 2 M. Uejima, T. Sato, D. Yokoyama, K. Tanaka and J.-W. Park, *Phys. Chem. Chem. Phys.*, 2014, **16**, 14244–14256.